Astronomy & Astrophysics

Regularized 3D spectroscopy with CubeFit: Method and application to the Galactic Center circumnuclear disk

ABSTRACT

Context. [illegible]

Aims. [illegible]

Methods. [illegible]

Results. [illegible]

Key words. [illegible]

1. Introduction

[illegible]

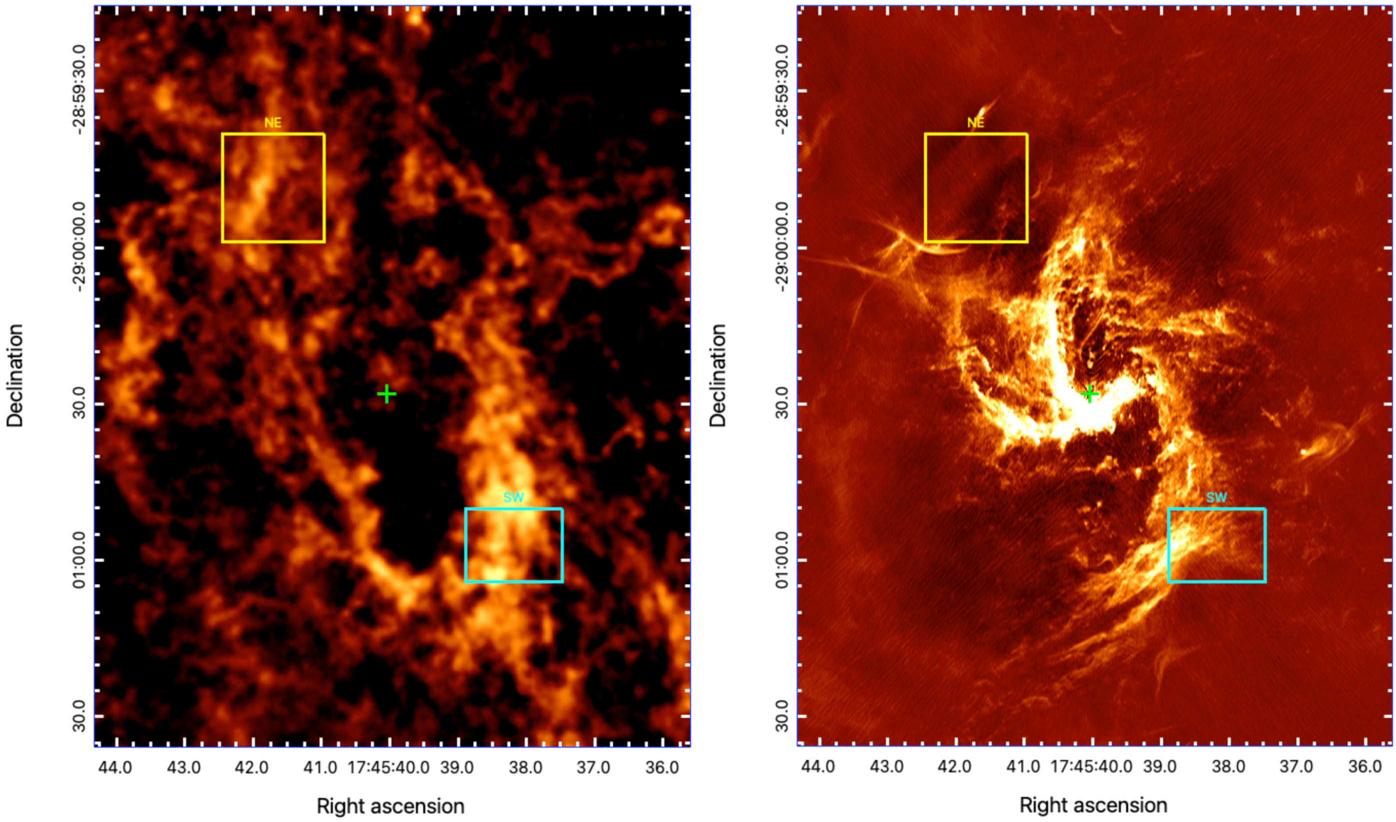

Fig. 1. [illegible] J [illegible]

[illegible]

[illegible] 10^7 cm^{-3} [illegible] 10^6 cm^{-3} [illegible] 10^6 to 10^8 cm^{-3} [illegible] 2 ± 0 [illegible] 10^4 $M_\odot$.

[illegible] H_2 [illegible] 0.1 [illegible]

[illegible]

[illegible]

2. Observations and data reduction

[illegible]

[illegible]

[illegible]

[illegible]

3. CubeFit: Data modeling with regularized parameter maps

[illegible]

Table 1. [illegible]

λ_{center} (μm)	n_{channels}	(μm)
[illegible]	[illegible]	[illegible]
[illegible]	[illegible]	[illegible]
[illegible]	[illegible]	[illegible]
[illegible]	[illegible]	[illegible]
[illegible]	[illegible]	[illegible]
[illegible]	[illegible]	[illegible]
[illegible]	[illegible]	[illegible]
[illegible]	[illegible]	[illegible]
[illegible]	[illegible]	[illegible]
[illegible]	[illegible]	[illegible]
[illegible]	[illegible]	[illegible]
[illegible]	[illegible]	[illegible]

Notes. [illegible]

Table 2. [illegible]

λ_{center} (μm)	n_{channels}	(μm)
[illegible]	[illegible]	[illegible]
[illegible]	[illegible]	[illegible]
[illegible]	[illegible]	[illegible]
[illegible]	[illegible]	[illegible]
[illegible]	[illegible]	[illegible]
[illegible]	[illegible]	[illegible]
[illegible]	[illegible]	[illegible]
[illegible]	[illegible]	[illegible]
[illegible]	[illegible]	[illegible]
[illegible]	[illegible]	[illegible]
[illegible]	[illegible]	[illegible]
[illegible]	[illegible]	[illegible]
[illegible]	[illegible]	[illegible]

[illegible]

3.1. Traditional independent 1D fits

[illegible]

3.2. An original regularized 3D fit

3.3. Test of the method on OH lines

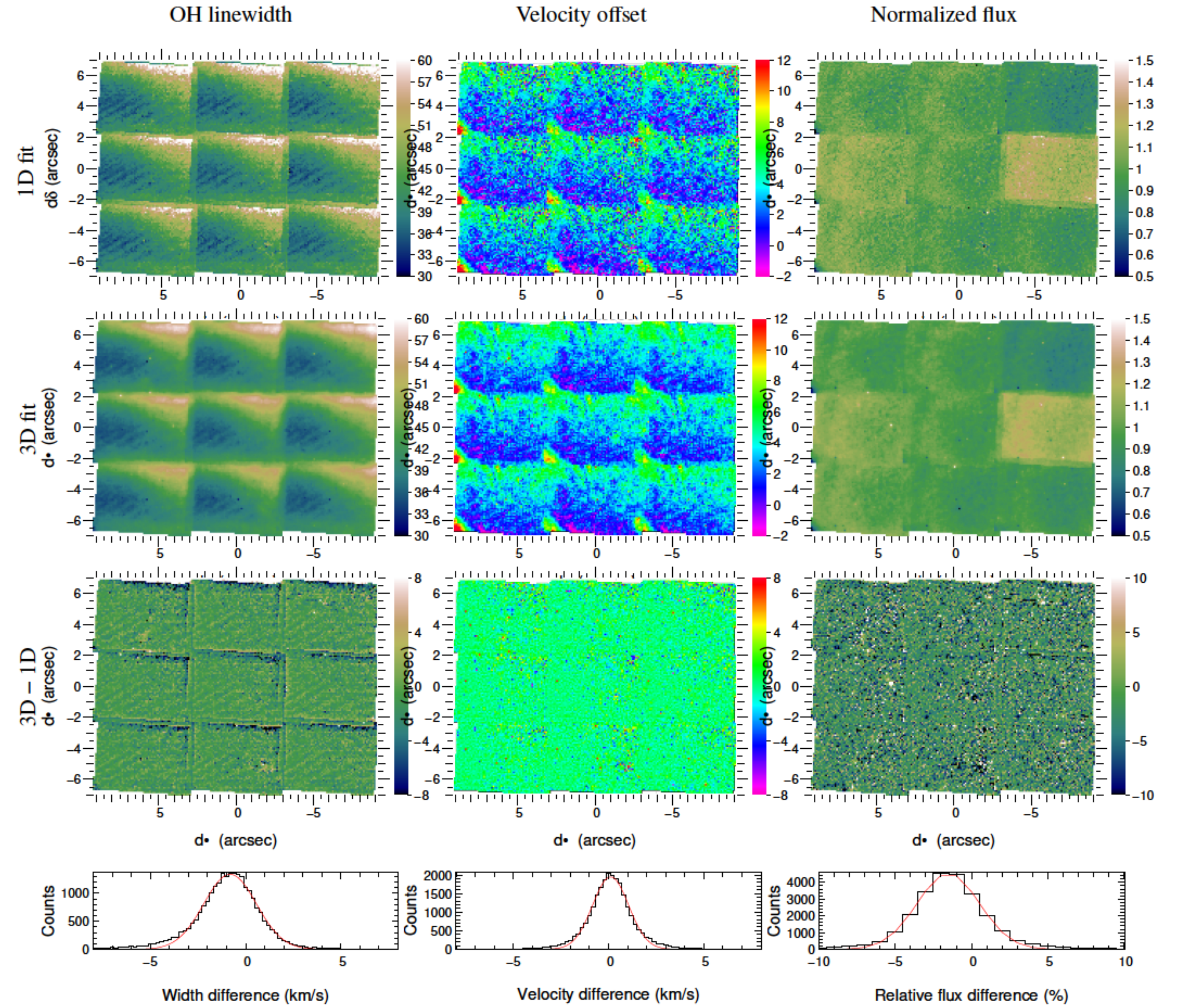

Fig. 2. Results of multiple OH line fits for the SW mosaic. *Left column:* linewidth (km s^{-1}). *Center column:* radial velocity offset (km s^{-1}). *Right column:* flux of the brightest line estimated as intensity times width normalized to the 1D fit median. *Top row:* median-filtered parameter maps from the 1D fit. *Second row from top*: regularized maps from the 3D fit. *Third row from top:* 3D parameter maps minus 3D fit (divided by 1D fit for flux). *Bottom row:* histograms of difference maps (black histograms) and Gaussian fits to those histograms (red curves). The moments of the Gaussian fits to the histograms are: median $\mu = -0.82$ km s^{-1} and width $\sigma = 1.38$ km s^{-1} for the linewidth difference; $\mu = 0.10$ km s^{-1} and $\sigma = 0.95$ km s^{-1} for the line velocity difference; and $\mu = -1.5\%$ and $\sigma = 2.0\%$ for the relative flux estimate difference.

1D-fit parameter maps are very well corrected by the regularization of CubeFit. For instance, artifacts from two very bright stars can be seen in the 1D flux map at $(\mathrm{d}\alpha, \mathrm{d}\delta) \simeq (-2'', -3'')$, and $(-2'', -5'')$. Finally, striping can also be seen in the 3D-fit velocity map subfields and can hardly be seen in the 1D-fit parameter map due to the additional noise.

The same analysis on the NE mosaic yields very similar results. In the rest of this paper, we fit the intrinsic width and radial velocity of various lines. To do so, we corrected the model for variable spectral resolution and wavelength calibration residuals by adding, pixel by pixel, the OH linewidth, $\boldsymbol{\sigma}_{\mathrm{OH}}(l,m)$ (in quadrature), and velocity offset, $\boldsymbol{v}_{\mathrm{OH}}(l,m)$, to the fitted linewidth and velocity:

$$\boldsymbol{\sigma}^{\mathrm{tot}}(l,m) = \sqrt{\boldsymbol{\sigma}(l,m)^2 + \boldsymbol{\sigma}_{\mathrm{OH}}(l,m)^2} \tag{9}$$

$$\boldsymbol{v}^{\mathrm{tot}}(l,m) = \boldsymbol{v}(l,m) + \boldsymbol{v}_{\mathrm{OH}}(l,m). \tag{10}$$

Since the S/N of the OH lines is so high, and in order to fully remove the sharp edges in the spectral resolution spatial variations, we used the results of the 1D fit for this purpose.

Further tests of the method are done in the next sections together with the analysis of the CND data and are summarized in Sect. 6.

4. Application to the CND data

To apply CubeFit to the (sky-subtracted) CND data, we chose to use line flux as a parameter for the Gaussian profile rather than line amplitude. The amplitude $\boldsymbol{I}(l,m)$ at any point is linked to the

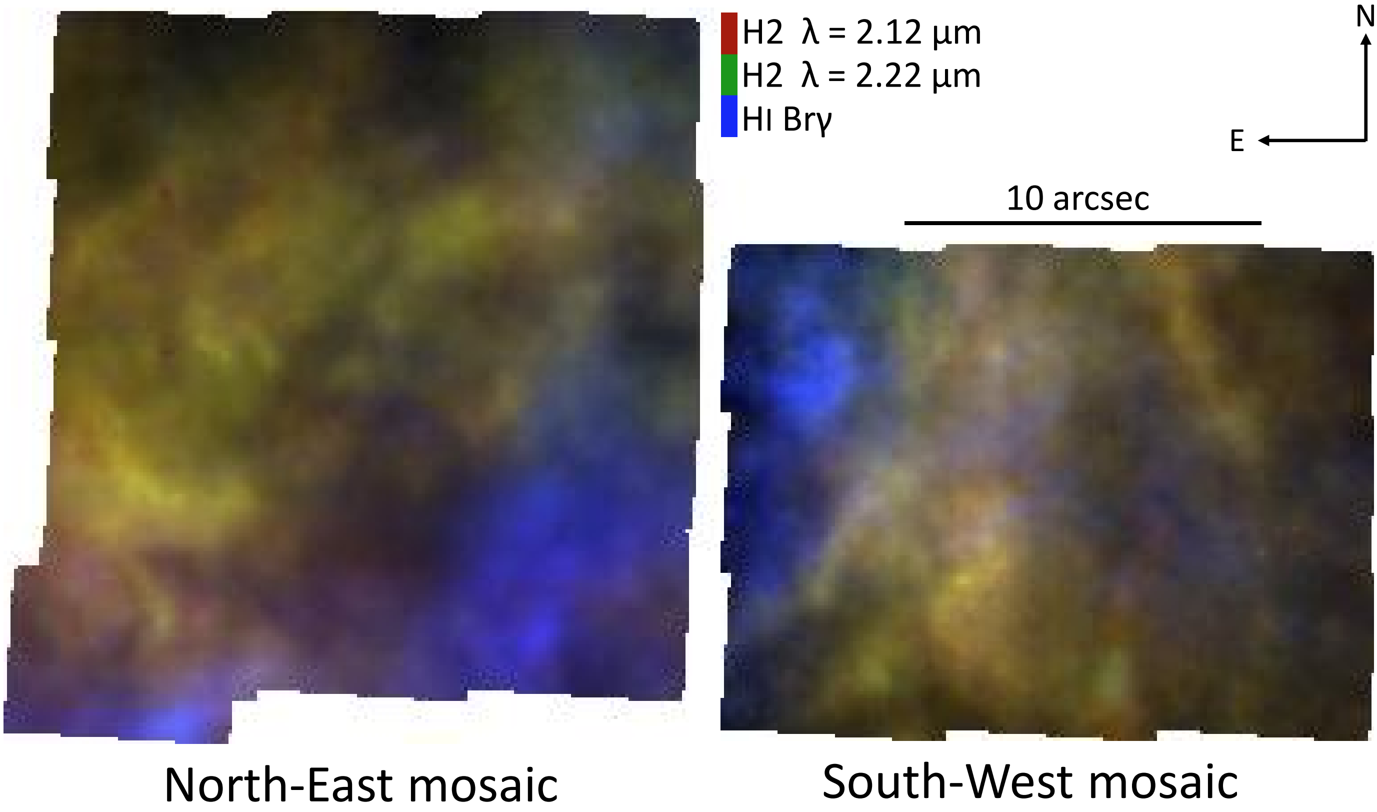
H2 λ = 2.12 µm
H2 λ = 2.22 µm
HI Brγ
N
E
10 arcsec
North-East mosaic
South-West mosaic

Fig. 3.

Table 3. [illegible]

[illegible]		$F_{\text{chan thresh}}$ [a]	Min(F) [b]	Max(F) [b]	σ_F [b]	σ_r [c]	[d]	[d]
N	H_2	3 68	8 5	67 4	0 88	1 1	1 8	0 95
N	B	1 72	3 2	30 2	0 46	–	1 5	2 6
SW	H_2	3 67	7 4	75 7	1 11	1 0	1 4	1 5
SW	B	1 86	3 0	53 6	0 42	–	1 1	1 6

Notes. x [illegible] x [illegible] [a] 10^{27} W [illegible] ^{2} [illegible] ^{2} [illegible] [b] 10^{27} W [illegible] ^{2} [illegible] ^{2}. [c] %. [d] km s^{-1}.

[illegible] B [illegible] H$_2$ [illegible]

$$F_{\text{chan}} = \frac{F}{\sqrt{2}} \qquad (4)$$

[illegible] F_{chan} [illegible] $F_{\text{chan thresh}}$ [illegible] $F_{\text{chan thresh}}$ [illegible]

[illegible] $\sqrt{4}$ [illegible] 2 [illegible]

[illegible] ($F_{\text{chan thresh}}$) [illegible] F_{chan} [illegible] $F_{\text{chan thresh}}$, [illegible] F [illegible]

[illegible] [6] [illegible] [7]) [illegible] H$_2$ [illegible] σ_F = 3.74 × 10^{27} W m^{-2} [illegible]^{2}, σ_r = 10%, [illegible] 9 4 km s^{-1}, [illegible] 9 2 km s^{-1}. [illegible] σ_F = 1 24 × 10^{26} W [illegible]^{2} [illegible]^{2}, σ_r = 15%, [illegible] 13 9 km s^{-1} [illegible] 23 7 km s^{-1}. [illegible]

4.1. NE mosaic

[illegible] 4 [illegible] 5 [illegible] H$_2$ [illegible] B [illegible] H I [illegible]

[illegible] B [illegible] 2 [illegible] 3

H$_2$ [illegible] H I [illegible] H$_2$ [illegible] H I [illegible] H$_2$ [illegible] 0 km s^{-1} [illegible] 60 km s^{-1} [illegible] H I [illegible] 0 km s^{-1} [illegible] 40 km s^{-1} [illegible] A [illegible] H$_2$ [illegible]

[illegible] H$_2$ [illegible] H I, [illegible] H$_2$ [illegible] σ_{H_2} = 50 km s^{-1}, [illegible] min $\bar{v}_{H_2}$ = 15 0 ± 0 6 km s^{-1} [illegible] max $\bar{v}_{H_2}$ = 83 4 ± 2 4 km s^{-1}. [illegible] H I, σ_B = 40 km s^{-1}, min $\bar{v}_B$ = 7 21 ± 1 48 km s^{-1} [illegible] max $\bar{v}_B$ = 63 57 ± 4 75 km s^{-1}. [illegible] 6 [illegible] 6 [illegible] 9 [illegible] H$_2$ [illegible] H^{2} [illegible] (d cos( ) d) = (6 3) [illegible] (3 1) [illegible] 7 [illegible] A [illegible]

4.2. SW mosaic

[illegible] 8 [illegible] 9 [illegible] H$_2$ [illegible] B [illegible] B [illegible] 4 [illegible] 3

H$_2$ [illegible] B [illegible]

---

6 [illegible]

7 [illegible]

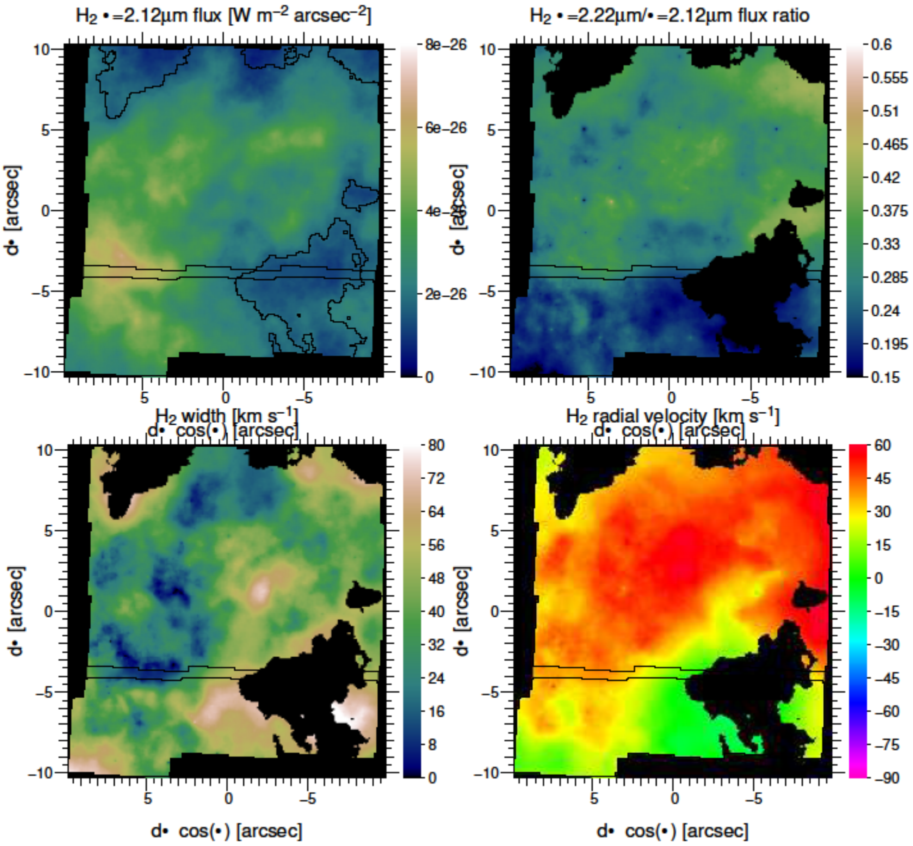

Fig. 4. Result of CubeFit on the NE mosaic for both H_2 lines. A black curve on the flux map delineates the amplitude threshold (see text). This region is masked out in the other maps. The four maps are, *from top left to bottom right*: H_2 $\lambda 2.12\,\mu$m line flux (F_{H_2}), flux ratio between the two lines (r_{H_2}), common intrinsic linewidth (σ_{H_2}), and common intrinsic radial velocity shift (v_{H_2}).

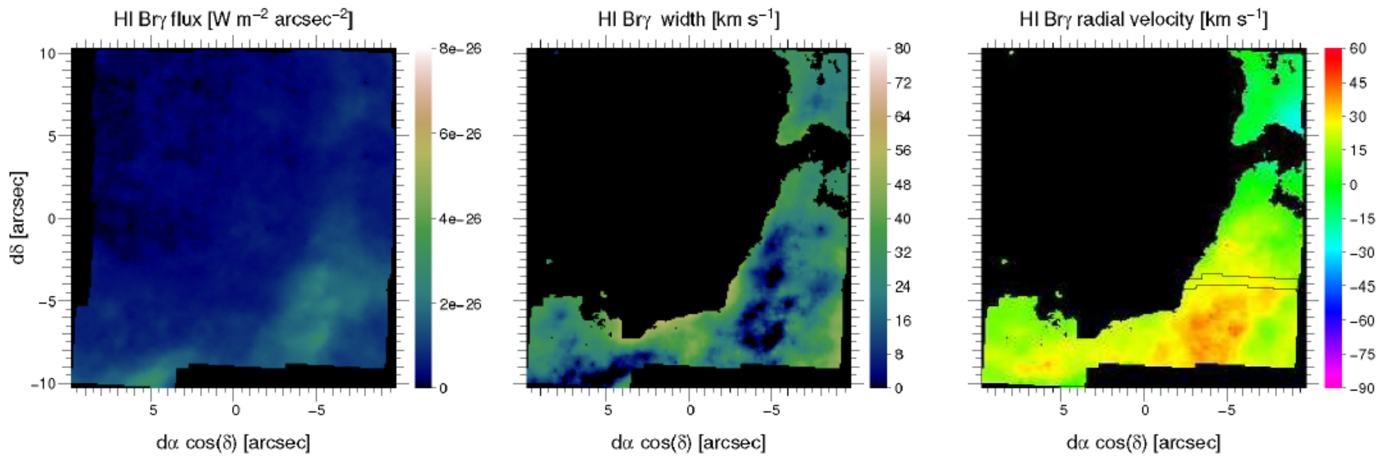

Fig. 5. Result of CubeFit on the NE mosaic for the Brγ line. A black curve on the flux map delineates the amplitude threshold (see text). This region is masked out in the other maps. The three maps are, *from left to right*: line flux ($F_{\mathrm{Br}\gamma}$), intrinsic width ($\sigma_{\mathrm{Br}\gamma}$), and intrinsic radial velocity shift ($v_{\mathrm{Br}\gamma}$).

features can be seen consistently in all parameter maps (clearly in the linewidth, flux and velocity maps, less clearly in the flux ratio map).

As in the NE field, linewidth is anticorrelated with flux, at least locally (Figs. 10 and 11). However, the brightest H_2 feature is not associated with a particularly strong local minimum in the width map. The filaments appear as deep valleys in the width map and ridges on the flux map. Two of the four such elongated features in the H_2 maps, labeled *A* and *B* in Fig. 8, are oriented in the southeast–northwest direction and parallel to the four features labeled *E* to *H* on the Brγ maps (Fig. 9). The H_2 and H II velocity maps also offer strong similarities: they can both be described as a plateau near $v \approx -30$ km s^{-1} occupying most of the field with the set of parallel filaments (*A*, *B* and *E* to *H*) at a significantly different velocity, near -80 km s^{-1}. We also note that Brγ is brightest along the eastern edge of the field, precisely where H_2 is not robustly detected.

In order to better probe the velocity field in the filaments, we extracted spectrograms (Figs. 12 and 13) along the four most prominent filaments of each map. The spectrograms extracted from the 3D cubes are similar to what would be achieved with a 0.3-arcsecond-wide long-slit spectrometer aligned on each filament. On slits *A* and *B*, the bulk of the emission has a velocity displacement of about -30 km s^{-1} with a drop to about -80 km s^{-1} on the eastern end (where the filamentary structures can be seen on the flux, linewidth and radial velocity maps). The (single-component) 3D fit yields a smooth transition between those two regions (white curve), especially for slit *B*. However,

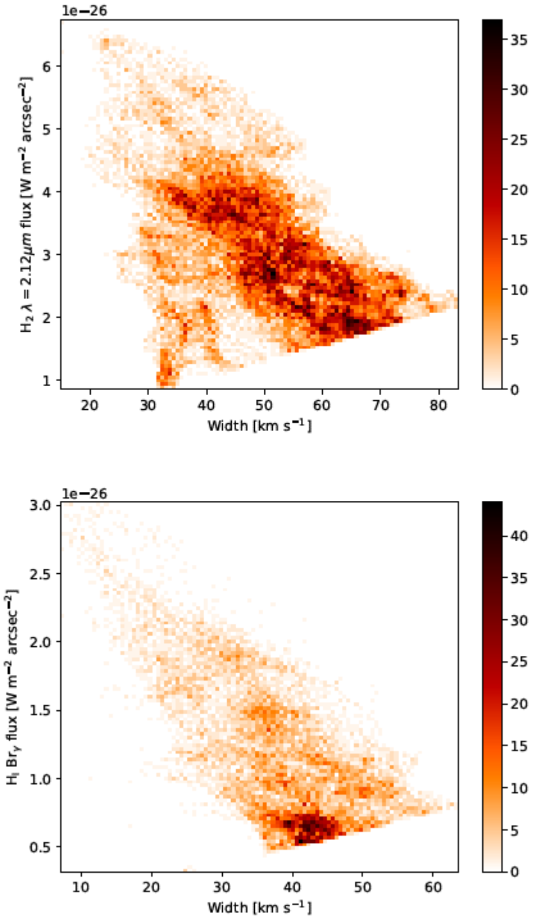

Fig. 6. Line flux vs. width density plot (arbitrary units) in the NE mosaic. *Top:* H_2 ($\lambda = 2.12$ μm). *Bottom:* H II. The threshold imposed on intensity results in a tilted lower selection boundary on this plot. For both species, the two quantities are anticorrelated. Although remarkable, the overall anticorrelation is not very tight. Denser regions in the plot could be the trace of individual clumps in the CND with a tighter local anticorrelation, modulated by variable foreground extinction.

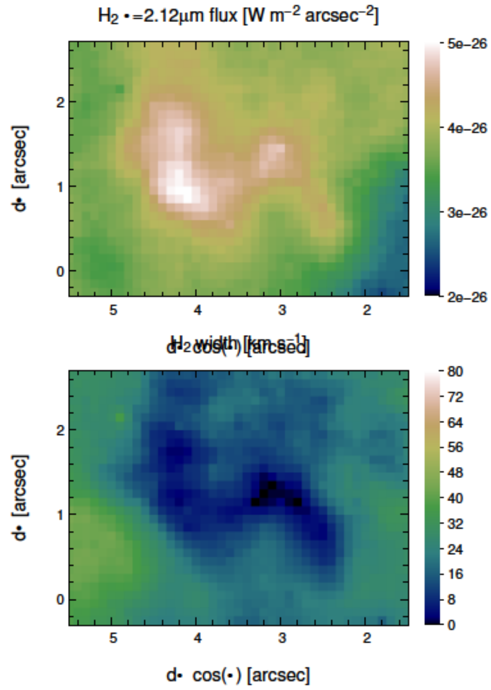

Fig. 7. Zoomed-in view of a feature in the NE H_2 mosaic ($\lambda = 2.12$ μm) line flux and width maps. The bright S-shaped ridge in the flux maps corresponds to a similarly shaped valley in the width map.

for both slits, another interpretation is also possible: that of two distinct, overlapping components (green, dash-dotted lines). The single component fit then gives a weighted average of the two actual components in the transition region. This interpretation is corroborated by looking at spectrogram *D*: Brγ emission is detected in this slit, but at $\simeq$−80 km s^{-1}, which is not well matched by the white line delineating the H_2 velocity. This indicates that H_2 and H II are separated into two components along the line-of-sight. Similarly, H_2 emission can be seen at slightly positive radial velocity on slits *E* to *G* (Fig. 13) where H II is again near −80 km s^{-1}. Conversely, in slit *H* (which is located about 1″ north of slit *B*), both species are detected at compatible velocities ($\simeq -80$ km s^{-1}).

5. Discussion

5.1. Comparison with radio maps

The two Brγ flux maps offer a striking resemblance to the Very Large Array (VLA) 6-centimeter continuum image (Fig. 1). This is most obvious for the SW mosaic where the Brγ emission occupies most of the field. The system of parallel elongated features seen in Fig. 9 (*E* to *H*) are seen very clearly in the VLA image as a detail in the Western Arc of the Minispiral. The fact that this system continues at larger distance from Sgr A* in H_2 (features labeled *A* and *B* in Fig. 8) is a confirmation that the Western Arc is the ionized inner edge of the CND (Vollmer & Duschl 1999; Nitschai et al. 2020). The same similarity between Brγ and 6-centimeter continuum also exists in the field of the NE mosaic but is less obvious because both are much less luminous there than in the SW field. However, one can still clearly see that the Brγ and 6-centimeter emission are concentrated along the southern and western sides of the NE field (see also Fig. 3), and a small filament in the 6-centimeter continuum image in the southeastern corner of the NE field can be recognized in the Brγ image.

Likewise, the two H_2 maps are very similar to the CS image from Fig. 1. The −80 km s^{-1} filamentary features seen in H_2 emission in the SW mosaic are evident in the CS image. The main H_2 features that can be seen in this mosaic are a thin filament running from the top center to the SW corner labeled *C* in Fig. 8, and a broad north-south ridge labeled *D*.

The fact that the morphology of many of the structures we identify in H_2 and H II match those observed in the radio (CS and continuum, respectively) represents a very strong, independent proof of the robustness of CubeFit results, even at small scales.

5.2. Bright features are compact

In both fields and in both species, we consistently see an anticorrelation between linewidth and flux, with large areas of low flux and broad linewidth contrasting with small regions of brighter flux and narrow linewidth. That can be explained in the following way. Hydrogen emission in H II regions is known to occur only (for H_2) or primarily (for Brγ) at the surface of clumps because clumps are usually optically thick in the ultra-violet. The fact that we see broad lines means that several clumps are stacked along the line-of-sight, so that one sees the integral of a velocity gradient or a velocity dispersion among clumps. Then, we can interpret the narrow line areas in the field as individual compact clumps that are particularly bright and therefore dominate the integral over the line-of-sight. Those clumps can be presumed to

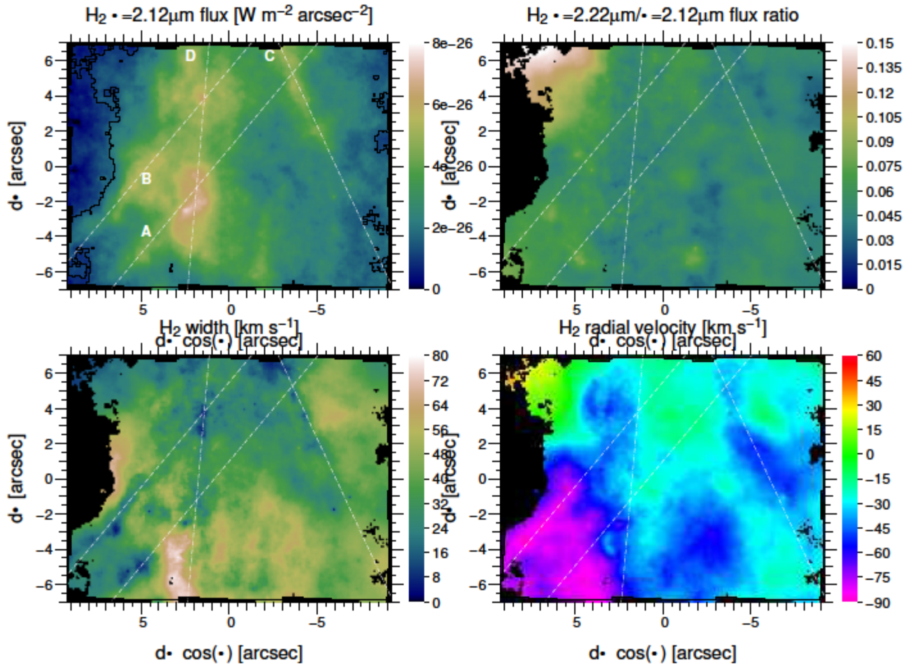

Fig. 8. H_2 in the SW mosaic; same panels as Fig. 4. Dash-dotted white lines indicate the locations of the virtual slits used in Fig. 12 and underline filamentary features.

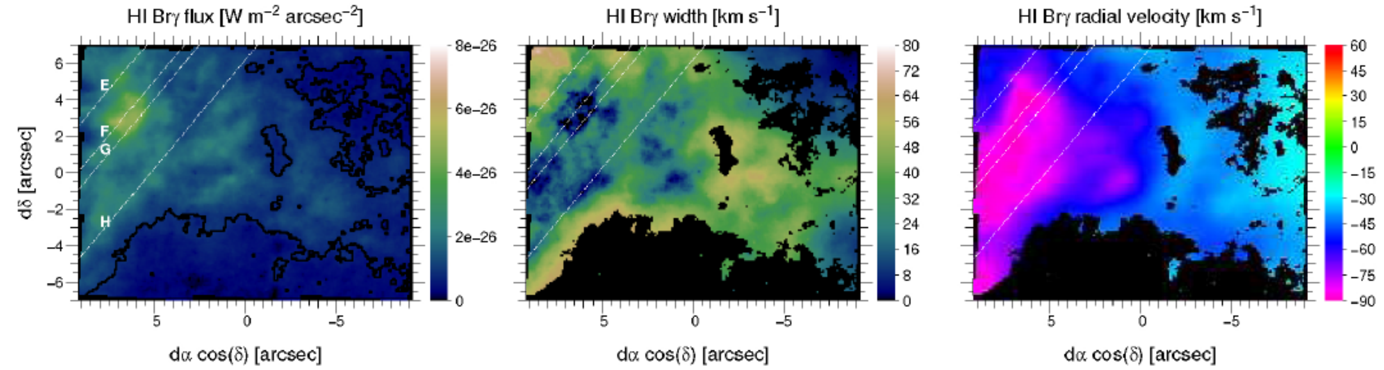

Fig. 9. Brackett-γ emission in the SW mosaic; same panels as Fig. 5. Dash-dotted white lines indicate the location of the virtual slits used in Fig. 13 and underline filamentary features.

be brighter as a consequence of a stronger ultraviolet field or a higher rate of collisional excitation. The particular H_2 lines that we probe in this paper do not allow us to discriminate between the two excitation mechanisms, both of which are possible in this environment (Ciurlo et al. 2016).

In this context, the brightest feature in the H_2 flux map for the SW field requires some attention as it is not associated with a strong local minimum of linewidth. Actually, this particular feature is at the intersection of the filaments labeled *A* and *D*. It is also at the transition between the -30 km s^{-1} plateau of the velocity map and the -80 km s^{-1} filaments. Therefore, this location is special. The appearance as the brightest flux maximum results from the overlap of several bright features. The velocity dispersion inside each of these individual features is small, as demonstrated by the width minima elsewhere in the *A* and *D* filaments, but the velocity dispersion among those individual features is large, which explains the overall large linewidth.

5.3. The filaments are thin clumps

Recognizing the Western Arc as the ionized inner edge of the CND raises the question of whether each clump is mostly molecular with an ionized surface, or whether some clumps are ionized and others neutral. In Figs. 8 and 9, filament *A* can be seen only in H_2, *E* to *G* can be seen only in H II, but *B* and *H*, which are less than 1″ apart, are essentially detected in both species. There are two ways to interpret those two features. It is possible that ridges *H* (seen in H II) and *B* (seen in H_2) trace two layers of different ionization states in a somewhat thick filament. Alternatively, it is also possible that they really are the trace of two distinct thin filaments, one of which is fully ionized and the other fully neutral. In this case, the fact that we also detect H II in slit *B* and H_2 in slit *H* could be attributed to spatial resolution and slit width (0.3″). The fact that we see only one such transition between the two ionization states, and not one in each filament, supports the interpretation that they are separate thin filaments. For the filaments presented here, the apparent shape of the emission feature (be it Brγ or one of the two H_2 lines) is a good representation of the actual shape of those clumps: rectilinear, thin ($\lesssim$0.3″ thickness) and long (reaching $\gtrsim$10″ length). This is in contrast with what has been seen in the central cavity (Ciurlo et al. 2019) where clumps appear to be only partially ionized. The observed elongation of the features we observe here is an argument against self-gravitating cloudlets.

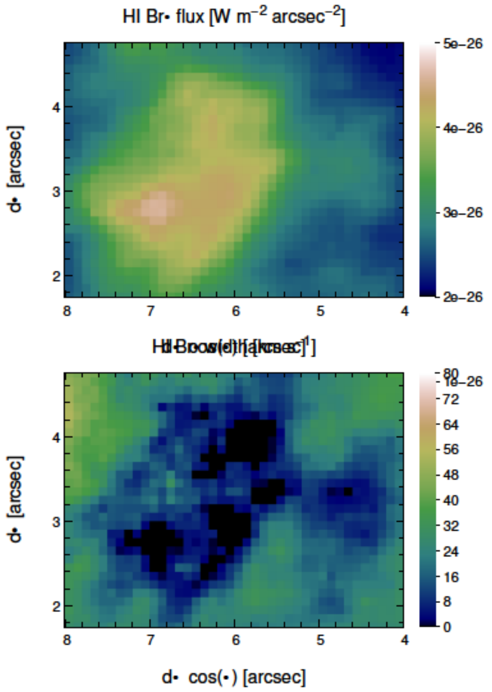

Fig. 10. Zoomed-in view of a feature in the SW mosaic: Brγ line flux and width maps.

6. Conclusion

The regularized 3D fitting method that we propose in Sect. 3 proves to be a robust way of estimating maps of physical parameters such as line flux, velocity dispersion, and radial velocity, recovering those parameters in regions where the local average per-voxel S/N is as low as ≈1. The resulting maps have the desired properties of being smooth while retaining sharp features (see, e.g., the sharp local minima in the linewidth maps). The uncertainties, estimated by repeating the same process over four independent data subsets, are very small; they correspond to what could be obtained after smoothing the data with a radius of ≈5 pixels (0.5″), which would have severely degraded the spatial resolution of the parameter maps (Fig. A.1). We validated the results of CubeFit and the associated uncertainties by comparing them with a more classical spaxel-by-spaxel 1D fit in Sect. 4. We provide another validation in Appendix A, where we compare the results of CubeFit with a more classical 1D fit at a few locations. With this comparison, we also demonstrate that variations in linewidth across the field, as estimated by the 3D method, are robust. This method has also been applied to another data set in a companion paper, Ciurlo et al. (2016), where we detected H_2 throughout the central cavity using the Spectrometer for Infrared Faint Field Imaging (SPIFFI) integral-field spectrometer at the European Southern Observatory (ESO) Very Large Telescope (VLT). Furthermore, in the application presented here we find small-scale features that corresponds to filaments and clumps observed in the radio and in other molecules. This provides a strong independent confirmation of the robustness of our findings with CubeFit.

We apply CubeFit to the Keck/OSIRIS data of the Galactic Center CND in Sect. 4. The linewidth map is a useful tool for identifying denser knots in the ISM, which appear as sharp local minima in the velocity dispersion. The ISM in the SW field is organized into two components: 1) a diffuse component near −30 km s^{-1} that contains only a few features, including two filaments oriented roughly in the north–south direction, and 2) a number of thin, compact, tidally sheared filaments, aligned along the orthoradial direction, with radial velocities near −80 km s^{-1}. These two components contain both H II and H_2, but each orthoradial filament contains only one of the two species, with the most ionized closer to the center of the nuclear star cluster. Those filaments are aligned with the filaments that are evident in the radio continuum image (Fig. 1) and with the local direction of the magnetic field (Dowell et al., priv. comm.). In contrast, shear seems to play less of a role in shaping the emission in the NE field, and the Brγ and H_2 emission seems to originate from distinct overlapping components. Here also, most of the surface is occupied by an optically thin medium emitting at low flux, with a few bright compact regions with presumably higher densities and optical depths.

Our observations therefore reveal a complex and clumpy environment, where low-density, high-filling factor material seems to coexist with higher-density, low-filling factor clumps that are tidally stretched and some of which are fully ionized. Those components have distinct kinematics, with radial velocities separated by ≃50 km s^{-1}. This picture is very different from the assumption of spherical, self-gravitating clumps, which has sometimes been invoked in past studies.

Observing the rest of the CND in the three lines used here would help determine whether our conclusions hold generally.

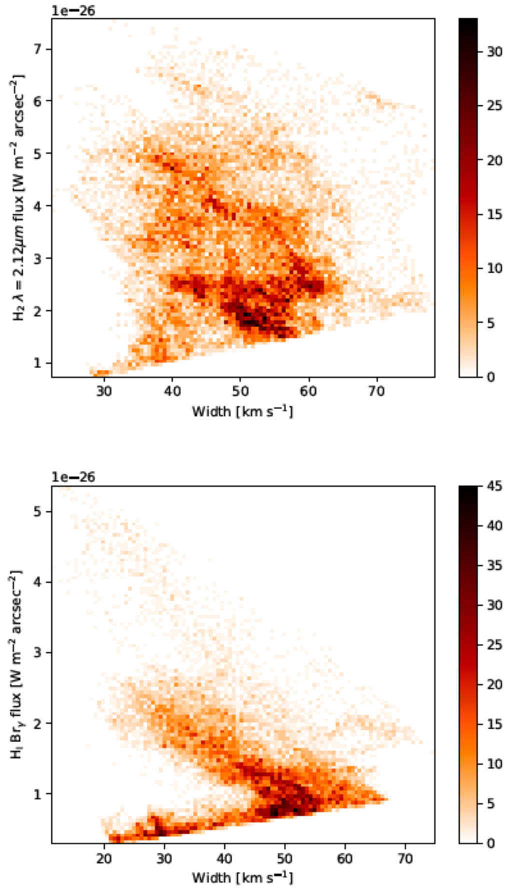

Fig. 11. Line flux vs. width density plot (arbitrary units) in the SW mosaic (see Fig. 6). The anticorrelation between line flux and width is quite remarkable in the *lower panel* (Brγ), where it takes the form of several narrow, densely populated streaks on the density plot. In the *top panel* (H_2), the anticorrelation is weaker than in the *bottom panel* and the density distribution is more diffuse, but one can still identify linear features, showing that such a correlation exists locally.

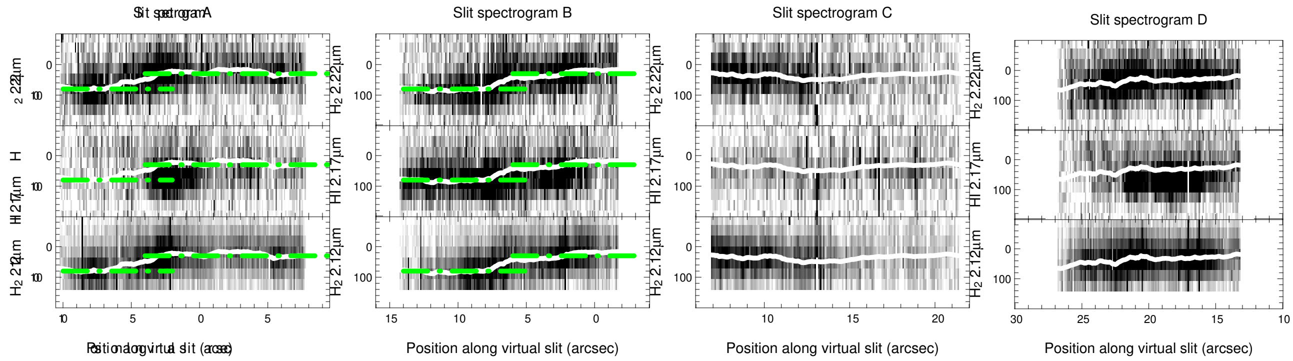

Fig. 12. [illegible]

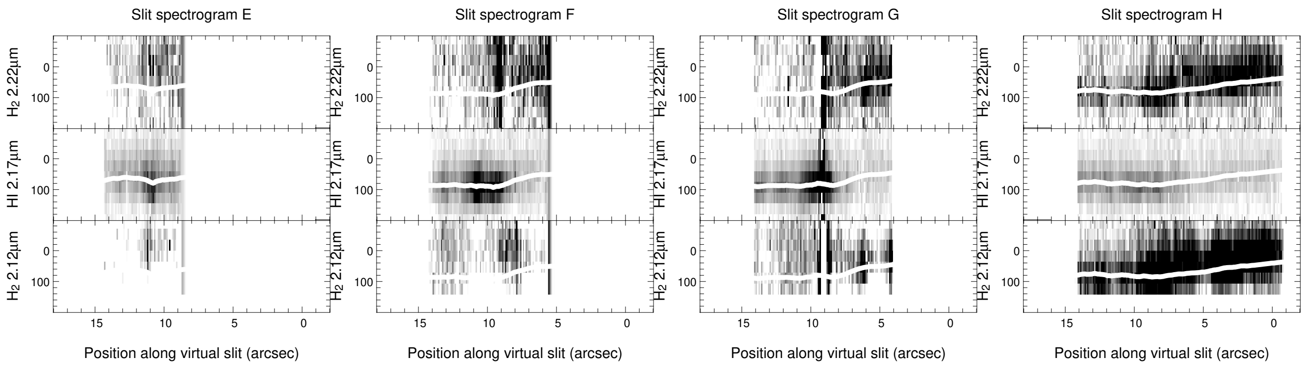

Fig. 13. [illegible]

[illegible]

References

[illegible]

Appendix A: Comparison with classical 1D method

In order to validate our method, we extracted a few spectra at typical places in the H_2 field by averaging spaxels over a 0.5″ radius (a median on 78 spaxels per aperture) and performed a classical 1D Gaussian fit on the H_2 λ 2.12 μm line in these spectra. The chosen location and spectra are displayed Fig. A.1. The average OH linewidth (weighted by F_{H_2}) over the same aperture is then subtracted in quadrature and the uncertainty is propagated from the uncertainty estimated by the fit itself. The corresponding estimate from the 3D fit and its uncertainty are given by the average of σ_{H_2} (Fig. 4) and σ_σ (Fig. B.1), also weighted by F_{H_2}. These 1D and 3D width measurements are listed in Table A.1 and agree very well. The classical 1D-fit approach corroborates the findings from CubeFit, confirming the intrinsic width variations over the field and confirming that the order of magnitude of our estimated uncertainties is correct.

We also performed the 1D fit over the entire SW cube, once on the original non-smoothed cube and once on a smoothed version of the cube where every spaxel contains the average spectrum over a 0.5″ radius as above. We again subtracted the OH linewidth in quadrature. A close-up of the width map derived from these two fits and from CubeFit is displayed Fig. A.2. Results from the 1D fit on the non-smoothed data contain high-resolution features but are very noisy. Smoothing the cube enhances the S/N significantly, at the cost of erasing the small-scale features. CubeFit brings the best of the two worlds together, keeping the high-resolution features while removing most of the noise, thus enhancing those small-scale features. The sharp astrophysical features that we discuss in Sect. 5, very clear with our method, are difficult to make out from the non-smoothed 1D fit and are smoothed out in the smoothed 1D fit. Another advantage of our method is its resilience on bad data points. A few bad voxels in the cube result only in individual spikes in our method (some can be seen in the flux ratio map for the NE mosaic, Fig. 4) while smoothing smears them over large areas.

Table A.1. Intrinsic H_2 linewidth (km s^{-1}) at the locations represented in Fig. A.1 as estimated by a 1D fit and CubeFit.

Location	1D fit	3D fit
A	23.8 ± 2.6	24.9 ± 1.5
B	25.9 ± 2.6	24.8 ± 1.9
C	35.3 ± 2.2	34.3 ± 1.9
D	46.7 ± 2.5	39.8 ± 1.5
E	41.9 ± 2.4	41.2 ± 2.3
F	39.4 ± 3.3	40.5 ± 1.4
G	41.3 ± 2.9	40.8 ± 1.3
H	43.6 ± 3.6	46.7 ± 1.7
I	50.7 ± 3.3	51.7 ± 1.4
J	56.3 ± 6.0	54.4 ± 1.6
K	52.5 ± 6.4	62.8 ± 2.0

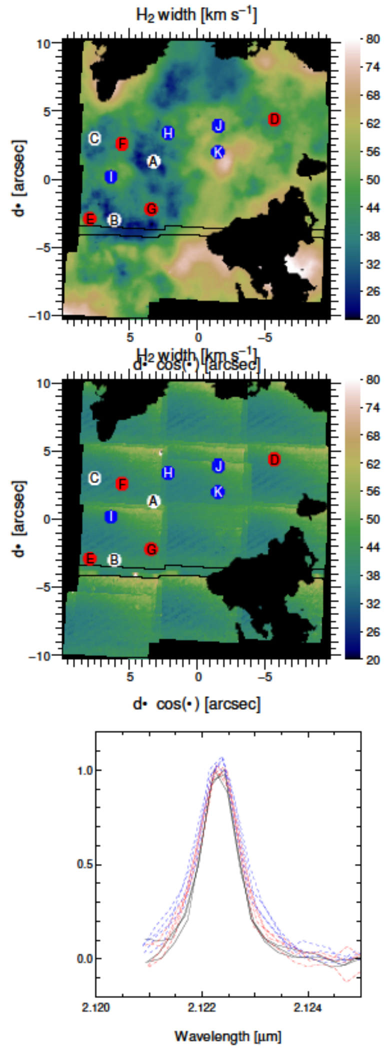

Fig. A.1. Variation in σ_{H_2} over the NE field. *Top:* H_2 linewidth map (as in Fig. 4). The colored dots mark the aperture over which spectra have been extracted. Three distinct colors correspond to three linewidth ranges: < 35 km s^{-1} in white and black, 35–42 km s^{-1} in blue, and > 42 km s^{-1} in red. *Middle:* corresponding OH linewidth map. *Bottom:* spectra extracted over each aperture, normalized according to the 1D Gaussian fit. The black spectra correspond to the white apertures, and the red and blue spectra correspond to the red and blue apertures. The corresponding widths are listed in Table A.1.

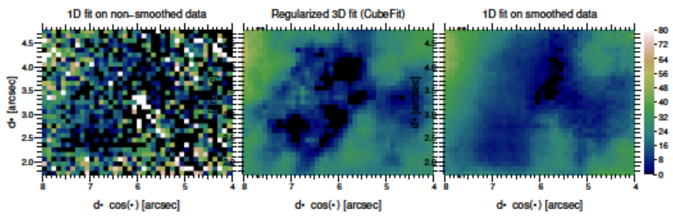

Fig. A.2. Close-up on three versions of the SW width map. *Left:* 1D fit on an original (non-smoothed) cube. *Center:* 3D fit with CubeFit. *Right:* 1D method fit on an aperture-smoothed cube.

Appendix B: Uncertainty maps

Figures B.1, B.2, B.3, and B.4 show the uncertainty maps associated with the parameter maps in Figs. 4, 5, 8, and 9, respectively. Median values over the considered field-of-view for each mosaic and specie are listed in Table 3.

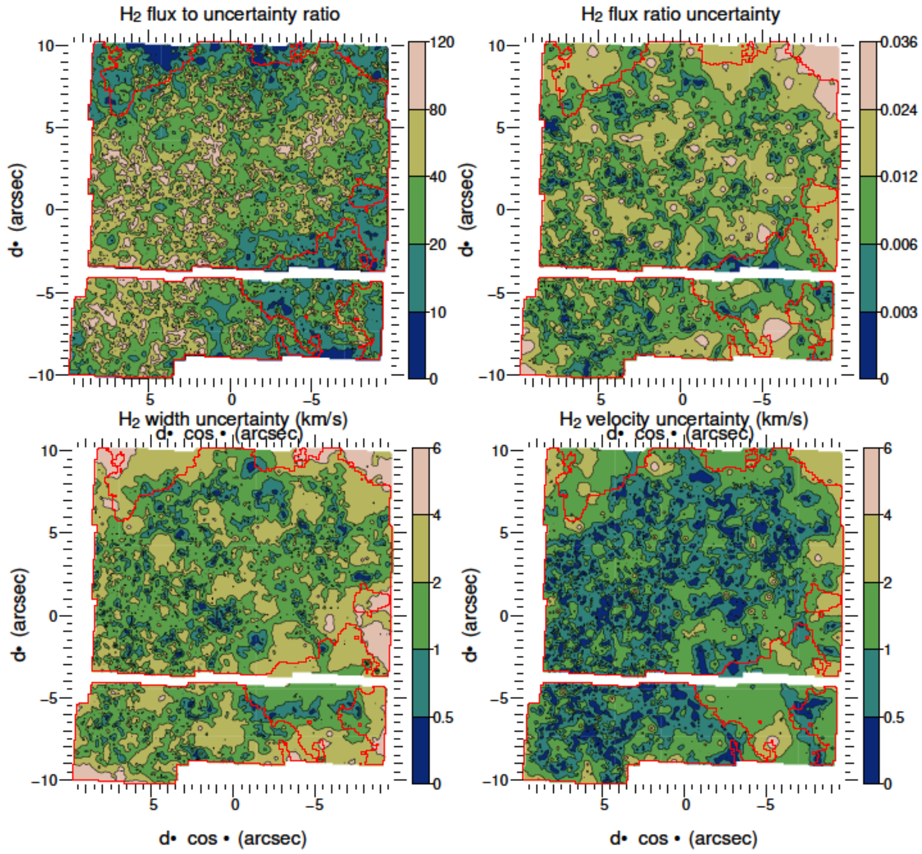

Fig. B.1. Uncertainty maps corresponding to Fig. 4. Red lines delineate the same amplitude threshold as on the flux map. We display the flux-to-flux uncertainty ratio rather than the uncertainty itself.

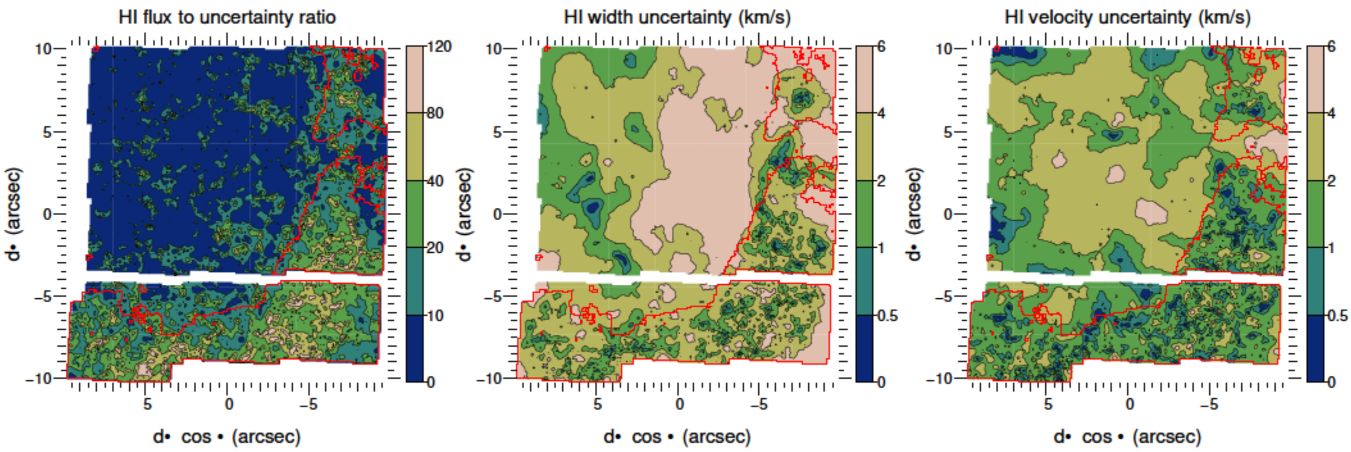

Fig. B.2. Uncertainty maps corresponding to Fig. 5. Red lines delineate the same amplitude threshold as on the flux map. We display the flux-to-flux uncertainty ratio rather than the uncertainty itself.

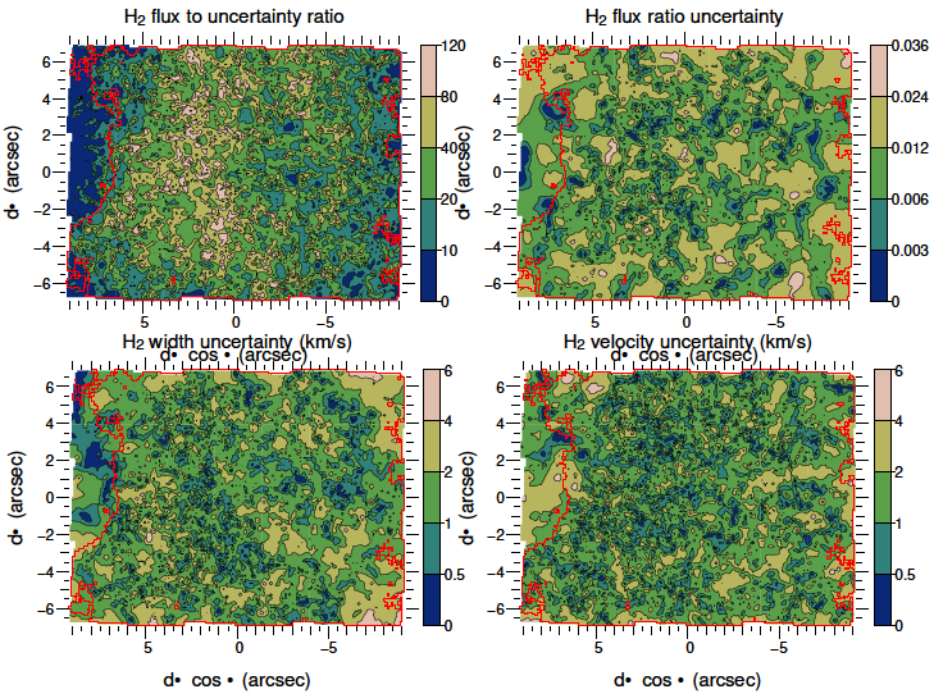

Fig. B.3. Uncertainty maps corresponding to Fig. 8. Red lines delineate the same amplitude threshold as on the flux map. We display the flux-to-flux uncertainty ratio rather than the uncertainty itself.

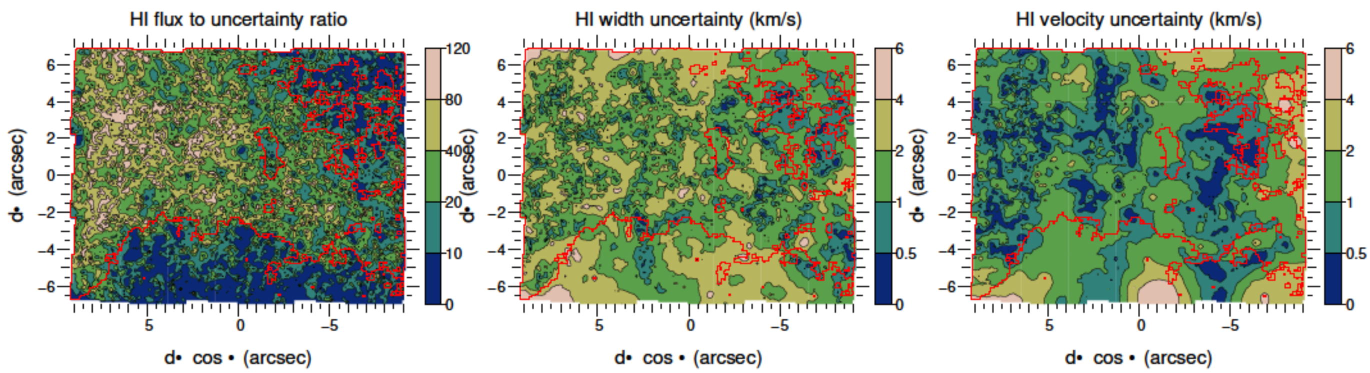

Fig. B.4. Uncertainty maps corresponding to Fig. 9. Red lines delineate the same amplitude threshold as on the flux map. We display the flux-to-flux uncertainty ratio rather than the uncertainty itself.